Progress In Electromagnetics Research B, Vol. 15, 1–29, 2009

SUB-NANOSECOND ELECTROMAGNETIC-MICROMAGNETIC DYNAMIC SIMULATIONS USING THE FINITE-DIFFERENCE TIME-DOMAIN METHOD

M. M. Aziz

School of Engineering, Computing and Mathematics
University of Exeter
Harrison Building, Exeter EX4 4QF, United Kingdom

Abstract—This paper presents an efficient and simple approach of implementing the Landau-Lifshitz-Gilbert (LLG) equation of magnetisation motion within the Finite-difference Time-domain (FDTD) method. This combined electromagnetic-micromagnetic simulation technique is particularly important for modeling electromagnetic interaction with lossy magnetic material in the presence of current and magnetic sources, particularly at very high frequencies. The efficient implementation involves simple two-point spatial interpolations that are applicable to two and three-dimensional FDTD grids, and uses a stable iterative algorithm for the time integration of the LLG equation. A ferromagnetic resonance numerical experiment on a rectangular Permalloy prism excited through its cross-section by a non-uniform pulse field from a transmission line was carried out for the purpose of verifying the combined FDTD-LLG computations. The numerical results were in good agreement with linearised analytical solutions of the LLG equation for uniform and non-uniform precession modes. This paper also presents a brief investigation on the use of non-staggered FDTD grid schemes to model magnetic material using the LLG equation, and indicates that the classical FDTD staggered scheme offers simplicity in implementation and more accuracy for modeling wave interaction with lossy magnetic material than the non-staggered schemes based on Maxwell's equations formulation.

1. INTRODUCTION

The Finite-difference Time-domain (FDTD) method is an explicit, second-order accurate finite-difference method for solving Maxwell's

Corresponding author: M. M. Aziz (M.M.Aziz@ex.ac.uk).

equations. Through its structure and implementation, it provides a flexible framework for the simulation of a wide range of electromagnetic phenomena, and provides almost infinite bandwidth due to its time domain nature [1]. Thus it provides a natural platform for dynamic and steady-state modelling of the interaction and coupling between electromagnetic waves from current and charge sources with non-linear magnetic material. This is of particular importance in the simulation of devices containing conductive magnetic materials with complex geometries and multi-layers with other dielectric and conductive materials operating at high frequencies. Examples include magnetic record and readout heads and ferrite loaded waveguides.

Two approaches have been adopted to solve electromagnetic problems involving magnetic materials using the FDTD method. The first approach involved using a frequency dependent tensor permeability that relates the magnetic flux density to the field strength in Maxwell's equations [2, 3]. This is a frequency domain approach which requires transformation into the time domain before inclusion into the FDTD formulation. It is limited to linearised forms of the equation of magnetisation motion without anisotropy and exchange fields and associated boundary conditions, and therefore does not yield information about the magnitude and distribution of magnetisation in the material.

In the second approach, Maxwell's equations are augmented with the Landau-Lifshitz-Gilbert (LLG) equation that describes the precessional motion of the magnetisation vector in a magnetic material under the influence of an effective field. Hence this formulation allows the inclusion of anisotropy and exchange effects, while the electromagnetic fields due to magnetic and/or electric charges and currents are evaluated naturally through the solution of Maxwell's equations. Hence this approach allows the simulation of complete magnetic based devices with dielectric and conductive layers, and is used in this paper. Previous work using this approach was limited to linear, small signal approximations of the LLG equation with [4, 5] or without damping [6–8], did not include magnetocrystalline anisotropy and exchange fields, with no treatment of magnetic boundary conditions, and used explicit schemes for the time integration of the LLG equation that were either inappropriate or unstable for small damping [8]. The previous work also used cumbersome and less accurate four-point spatial interpolations to evaluate the fields and magnetisations due to the staggered nature of the FDTD grid [4, 5, 7, 8]. Detailed work by Vacus and Vukadinovic [9] was carried out to solve the nonlinear system of the LLG equation and Maxwell's equations using the FDTD method that incorporated anisotropy and

exchange fields and using implicit schemes, but used a numerically dispersive, unstaggered FDTD grid for the implementation, which is not appropriate for studying dynamic wave interaction with magnetic material.

The aims of this work are therefore to provide an efficient and simple implementation of the discretised LLG equation (including anisotropy and exchange fields) within the FDTD grid, referred to here as the FDTD-LLG scheme, and to present the complete stable algorithm for the solution of the nonlinear system of the LLG and Maxwell's equations. Driven by the desire to simplify the staggered spatial discretisation of Maxwell's equations to conform to the unstaggered nature of the LLG equation, this paper also presents a discussion on a brief investigation that was carried out on the use of unstaggered FDTD schemes for the modeling and simulation of lossy magnetic material.

Section 2 of this paper presents the mathematical models of the electromagnetic and micromagnetic equations involved. The finite-difference discretisation and time marching algorithms for the solution of Maxwell's and the LLG equations within the FDTD framework along with the proposed efficient discretisation scheme are detailed in Section 3. In Section 4, a numerical experiment is presented whereby a thin rectangular Permalloy prism is excited by a pulse field from transmission lines, and compared with approximate analytical solutions of the problem to validate the numerical computations of the combined FDTD-LLG scheme. An overview of the outcomes and possible extensions and improvements to the FDTD-LLG scheme will be discussed in Section 5, including a discussion on the potential use of two unstaggered schemes based on Maxwell's equations for modeling and simulation of lossy magnetic material.

2. MATHEMATICAL MODELS

2.1. Maxwell's Equations

In the MKS system of units, Maxwell's curl equations for a general lossy, dispersive medium are:

$$\frac{\partial \mathbf{B}}{\partial t} = -\nabla \times \mathbf{E} \tag{1}$$

$$\varepsilon \frac{\partial \mathbf{E}}{\partial t} = \nabla \times \mathbf{H} - \sigma \mathbf{E} \tag{2}$$

where $\mathbf{H}$ is the magnetic field, $\mathbf{E}$ is the electric field, ε is the permittivity of the medium, and σ is the electrical conductivity. The

magnetic flux density $\mathbf{B}$ is related to the magnetisation in a magnetic medium through the constitutive relation:

$$\mathbf{B} = \mu_0(\mathbf{M} + \mathbf{H}) \tag{3}$$

where μ_0 is the permeability of free space.

For simplicity, the electromagnetic fields presented in this paper are limited to two dimensions in transverse-magnetic mode with respect to z (TMz). However, the work presented here is directly applicable to the transverse-electric (TEz) and full three-dimensional modes. In the TMz mode, Maxwell's curl equations reduce to:

$$\frac{\partial B_x}{\partial t} = -\frac{\partial E_z}{\partial y} \tag{4}$$

$$\frac{\partial B_y}{\partial t} = \frac{\partial E_z}{\partial x} \tag{5}$$

$$\varepsilon\frac{\partial E_z}{\partial t} = \frac{\partial H_y}{\partial x} - \frac{\partial H_x}{\partial y} - \sigma E_z \tag{6}$$

2.2. The Landau-Lifshitz-Gilbert Equation

The Landau-Lifshitz equation of magnetisation motion with the Gilbert damping term is used in this work and is given by [10]:

$$\frac{d\mathbf{M}}{dt} = -|\gamma|(\mathbf{M} \times \mathbf{H}_{\mathit{eff}}(\mathbf{M})) + \frac{\alpha}{|\mathbf{M}|}\left(\mathbf{M} \times \frac{d\mathbf{M}}{dt}\right) \tag{7}$$

where $\gamma = 1.75882 \times 10^{11}\mu_0\,(\mathrm{m{\cdot}Hz/A})$ is the gyromagnetic ratio, α is the Gilbert damping coefficient, $|\mathbf{M}| = M_s$ is the saturation magnetisation and $\mathbf{H}_{\mathit{eff}}$ is the effective field given by:

$$\mathbf{H}_{\mathit{eff}}(\mathbf{M}) = \mathbf{H}_{\mathit{app}} + \mathbf{H}(\mathbf{M}) + \mathbf{H}_k(\mathbf{M}) + \mathbf{H}_{ex}(\mathbf{M}) \tag{8}$$

The effective field includes the following field contributions:

2.2.1. Applied Field, $\boldsymbol{H}_{app}$

This is a user-defined field inside the magnetic medium and can be static or transient, uniform or non-uniform.

2.2.2. Maxwell Field, $\boldsymbol{H}$

Fields generated from the solution of Maxwell's equations and internal to the magnetic medium. These include fields due to currents and magnetic sources such as demagnetising fields and eddy current fields.

2.2.3. Exchange Field, $\boldsymbol{H}_{ex}$

These fields try to align neighbouring magnetic spins into the same direction in the magnetic material. For nearest neighbour interactions, the exchange field is given by [11]:

$$\mathbf{H}_{ex} = \frac{2A}{\mu_0 M_s^2} \nabla^2 \mathbf{M} \tag{9}$$

where A is the exchange constant, and ∇^2 is the Laplacian operator.

2.2.4. Anisotropy Field, $\boldsymbol{H}_k$

A uniaxial magnetocrystalline anisotropy is assumed in this work with field:

$$\mathbf{H}_k = \frac{-2K_u}{\mu_0 M_s^2} (\mathbf{M} \cdot \mathbf{u})\mathbf{u} \tag{10}$$

where K_u is the anisotropy constant, and $\mathbf{u}$ is a unit vector parallel to the anisotropy axis.

In the absence of surface anisotropy, the exchange boundary condition for the LLG equation in (7) is [12]:

$$\frac{\partial \mathbf{M}}{\partial \mathbf{n}} = 0 \quad (\text{or} \quad \mathbf{n} \cdot \nabla \mathbf{M} = 0) \tag{11}$$

where $\mathbf{n}$ is the vector normal to the surface of the magnetic material.

3. NUMERICAL IMPLEMENTATION

3.1. The Finite-Difference Time-Domain (FDTD) Method

In the FDTD method, the fundamental spatial unit is the Yee cell [13], shown in Fig. 1 with side lengths Δx, Δy, and Δz. Each $\mathbf{E}$ field component in the centre of the Yee cell is evaluated from the curl of the four surrounding magnetic field components, while each $\mathbf{H}$ field component is evaluated using the curl of the four neighbouring electric field components. The electric and magnetic field components are displaced from each other in space by half a cell length. This field arrangement naturally satisfies the fields' boundary conditions at the interfaces of different materials and therefore boundary conditions need not be enforced [1, 13].

The front face of the unit cell in Fig. 1 represents a TMz structure, followed by a TEz structure half a cell into the negative z-direction. As previously indicated, this paper focuses on the TMz mode grid

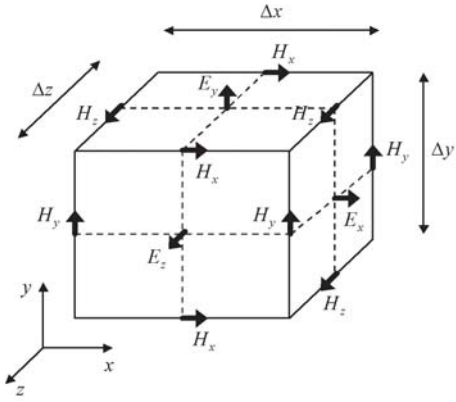

Figure 1. Fundamental Yee cell in the FDTD method.

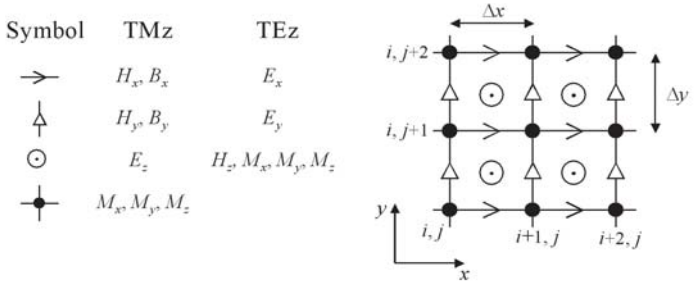

Figure 2. Two-dimensional FDTD grid showing TMz and TEz field symbols, including the proposed placement of the magnetisation vector at the cross points of the grid cells.

for simplicity, but nevertheless references to the TEz and three-dimensional grids will be made, as the proposed implementation is applicable to these modes. Fig. 2 shows a FDTD grid made from a number of Yee cells in two dimensions, along with the field components in the TMz and TEz modes.

The convention used here to represent the discretised field component f in two dimensions is $f|_{i,j}^{n} = f(i\Delta x, j\Delta y; n\Delta dt)$ where the subscripts i and j are integers representing spatial grid locations in the x and y direction respectively, and the superscript n is an integer representing the increment of the time step Δt. For example, discretisation of Equation (4) using second-order accurate, central

differences at time step n yields:

$$\left.\frac{\partial B_x}{\partial t}\right|_{i+1/2,j}^{n} \approx -\left(\frac{E_z|_{i+1/2,j+1/2}^{n} - E_z|_{i+1/2,j-1/2}^{n}}{\Delta y}\right) \tag{12}$$

Time integration is achieved using a second-order accurate leapfrog algorithm [13] where the magnetic flux density B in Equations (4) and (5) is evaluated at time step n, which is then used to evaluate the electric field $\mathbf{E}$ at time step $n + 1/2$ in (6) and so forth. Applying this discretisation scheme and evaluating the time average of the electric field from:

$$E_z|^{n+1/2} = \frac{E_z|^{n} + E_z|^{n+1}}{2}$$

yields the explicit, discretised update equations for the TMz field components of Equations (4), (5) and (6):

$$B_x|_{i+1/2,j}^{n+1/2} = B_x|_{i+1/2,j}^{n-1/2} - \frac{\Delta t}{\Delta y}\left[E_z|_{i+1/2,j+1/2}^{n} - E_z|_{i+1/2,j-1/2}^{n}\right] \tag{13}$$

$$B_y|_{i,j+1/2}^{n+1/2} = B_y|_{i,j+1/2}^{n-1/2} + \frac{\Delta t}{\Delta x}\left[E_z|_{i+1/2,j+1/2}^{n} - E_z|_{i-1/2,j+1/2}^{n}\right] \tag{14}$$

$$\begin{aligned} E_z|_{i+1/2,j+1/2}^{n+1} \;=\; & \left(\frac{1+\sigma\Delta t/(2\varepsilon)}{1-\sigma\Delta t/(2\varepsilon)}\right) E_z|_{i+1/2,j+1/2}^{n} \\ & + \frac{\Delta t}{(1+\sigma\Delta t/(2\varepsilon))} \times \left[\frac{H_y|_{i+1,j+1/2}^{n+1/2} - H_y|_{i,j+1/2}^{n+1/2}}{\Delta x}\right. \\ & \left. - \frac{\left(H_x|_{i+1/2,j+1}^{n+1/2} - H_x|_{i+1/2,j}^{n+1/2}\right)}{\Delta y}\right] \end{aligned} \tag{15}$$

where it is understood that σ and ε are located in space at the same location as their respective field components. The magnetic field $\mathbf{H}$ in (15) is computed from (13) and (14) using the constitutive relation in (3):

$$\mathbf{H}^{n+1/2} = \begin{cases} \dfrac{\mathbf{B}^{n+1/2}}{\mu_0} - \mathbf{M}^{n+1/2} & \text{inside magnetic material} \\ \dfrac{\mathbf{B}^{n+1/2}}{\mu_0\mu_r} & \text{outside magnetic material} \end{cases} \tag{16}$$

where μ_r is the relative permeability.

Equation (16) requires **M** to be located at the same location in space as **H** and **B** (i.e., displaced by half-cell lengths). This requirement is in contradiction with the localised nature of the LLG equation where the magnetisation and field components need to be evaluated at the same location in space. If **M** is positioned at the same location in space as **H** and **B** then four-point spatial interpolations would be necessary to determine each magnetisation and field component at each of the half-cell displaced neighbouring field locations in the Yee cell for the numerical computations [4, 5, 8]. This procedure is less accurate, and makes the numerical implementation, in general, and of magnetic boundary conditions in particular more complex as the boundary of the magnetic material is not well defined.

A more efficient and simpler approach is proposed here where the magnetisation vector **M** is positioned at one point in space: at the corners of the Yee cell as indicated in Fig. 2. This approach conforms to the local nature of the LLG equation where all magnetisation components are evaluated at the same point in space, is easier to implement as only simple and more accurate two-point spatial interpolations are required, and the magnetic material boundaries are well defined. For example, to determine the value of M_x at the same location as H_x or $B_x(i+1/2, j)$ in (16), the following two-point interpolation is used:

$$M_x|_{i+1/2,j}^{n+1/2} = \frac{M_x|_{i+1,j}^{n+1/2} + M_x|_{i,j}^{n+1/2}}{2}$$

Similar interpolations can be carried out to evaluate the remaining magnetisation components at the same location as the magnetic field components for the FDTD update equations. Placing the magnetisation vectors at the corners of the FDTD cells, moreover, allows the same simple two point interpolations to be used in TEz and three-dimensional FDTD grids.

Square Yee cells are adopted in this work for simplicity with $\Delta x = \Delta y$. The spatial increment Δx in the FDTD grid is chosen to sufficiently sample the shortest wavelength in the system (normally determined by the bandwidth of the source), and to accurately model the smallest dimension and/or physical and electromagnetic phenomenon in the simulated materials (such as skin depth, exchange length or domain wall width in a magnetic material).

The numerical stability of the FDTD leapfrog time marching scheme is well understood and imposes the following restriction on the time step size, known as the Courant limit, for stable time

integration [1, 13]:

$$\Delta t \leq \frac{\Delta x}{c\sqrt{dim}} \tag{17}$$

where c is the speed of light in vacuum, and *dim* is the dimensionality of the system and is equal to 2 for the TMz mode considered here.

To absorb outgoing waves and prevent them from reflecting back into the simulation space and causing errors, the split-field, perfectly matched layer (PML) formulation of Berenger [14] is implemented throughout this work.

3.2. Time Integration of the LLG Equation

The time derivatives in the LLG equation in (7) at time step n may be approximated using central differences yielding:

$$\begin{aligned}\frac{\mathbf{M}^{n+1/2} - \mathbf{M}^{n-1/2}}{\Delta t} &= -|\gamma|(\mathbf{M}^n \times \mathbf{H}^n_{\mathit{eff}}(\mathbf{M}^n)) \\ &\quad + \frac{\alpha}{M_s}\left(\mathbf{M}^n \times \frac{\mathbf{M}^{n+1/2} - \mathbf{M}^{n-1/2}}{\Delta t}\right)\end{aligned}$$

Rewriting the time derivative term on the right-hand-side as:

$$\frac{\mathbf{M}^{n+1/2} - \mathbf{M}^{n-1/2}}{\Delta t} = \frac{(\mathbf{M}^{n+1/2} + \mathbf{M}^{n-1/2}) - 2\mathbf{M}^{n-1/2}}{\Delta t}$$

and expressing the magnetisation on both sides of the LLG equation at time step n using the average:

$$\mathbf{M}^n = \frac{\mathbf{M}^{n+1/2} + \mathbf{M}^{n-1/2}}{2}$$

yields a second-order accurate update equation for the magnetisation at time step n:

$$\mathbf{M}^n = \mathbf{M}^{n-1/2} - \mathbf{M}^n \times \left(\frac{|\gamma|\Delta t}{2}\mathbf{H}^n_{\mathit{eff}}(\mathbf{M}^n) + \frac{\alpha}{M_s}\mathbf{M}^{n-1/2}\right) \tag{18}$$

where the effective field $\mathbf{H}_{\mathit{eff}}$ is given by Equation (8).

Equation (18) cannot be solved explicitly since the evaluation of the effective field requires $\mathbf{M}^n$ on the right-hand-side which is not available. The non-linear system of Maxwell and LLG equations therefore cannot be solved using an explicit scheme (unless anisotropy and exchange fields are ignored). An explicit numerical scheme based

on extrapolation has been proposed in [8], however this scheme was found to be inherently unstable for small damping and is therefore not appropriate for dynamic and steady-state simulations.

In this work, an implicit and stable iterative numerical scheme [9, 15] will be employed to solve the LLG equation in (18). The complete time stepping algorithm for the solution of the non-linear system of Maxwell's and the LLG equations is presented here in detail including the coupling of the magnetisation to the fields in Maxwell's equations using the proposed interpolation scheme, and implementation of magnetic boundary conditions. The algorithm is:

1) Evaluation of $\mathbf{B}^{n+1/2}$ from Maxwell's Equations (13) and (14) using the previous computed values of the electric field $\mathbf{E}^n$ and magnetic flux density $\mathbf{B}^{n-1/2}$. Then the magnetic flux density at time step n can be computed from the time average:

$$\mathbf{B}^n = \frac{\mathbf{B}^{n+1/2} + \mathbf{B}^{n-1/2}}{2}$$

2) Evaluation of $\mathbf{B}^n$ at the locations of the $\mathbf{M}$ (i.e., cell corners) using interpolations. For example, B_x is determined at the cell corner where M_x is located using the two-point spatial interpolation:

$$B_x|^n_{i,j} = \frac{B_x|^n_{i+1/2,j} + B_x|^n_{i-1/2,j}}{2}$$

Similar interpolation is performed to determine $B_y|^n_{i,j}$.

3) Iterative solution of the LLG equation in (18) re-written here in terms of the iteration number r:

$$[\mathbf{M}^n]^r = \mathbf{M}^{n-1/2} - [\mathbf{M}^n]^r \times \left(\frac{|\gamma|\Delta t}{2} \mathbf{H}^n_{\mathit{eff}}([\mathbf{M}^n]^{r-1}) + \frac{\alpha}{M_s} \mathbf{M}^{n-1/2} \right)$$

with initial values $\mathbf{M}^n = \mathbf{M}^{n-1}$ and $\mathbf{H}^n_{\mathit{eff}} = \mathbf{H}^{n-1}_{\mathit{eff}}$.

Begin iteration r:

i) Solve Equation (18) explicitly for $[\mathbf{M}^n]^r$, using previous values $\mathbf{H}^n_{\mathit{eff}}([\mathbf{M}^n]^{r-1})$ and $\mathbf{M}^{n-1/2}$ as constants, from [9]:

$$[\mathbf{M}^n]^r = \frac{\mathbf{M}^{n-1/2} + (\mathbf{a} \cdot \mathbf{M}^{n-1/2})\mathbf{a} - \mathbf{a} \times \mathbf{M}^{n-1/2}}{1 + |\mathbf{a}|^2} \tag{19}$$

where $\mathbf{a} = -\left(\frac{|\gamma|\Delta t}{2} \mathbf{H}^n_{\mathit{eff}}([\mathbf{M}^n]^{r-1}) + \frac{\alpha}{M_s} \mathbf{M}^{n-1/2} \right)$

ii) Update the magnetic boundary condition described by Equation (11) at the material interfaces using forward and backward

differences. For example, on the left hand boundary of the TMz grid in Fig. 2, the magnetic boundary condition can be approximated by the forward difference:

$$\frac{\partial \mathbf{M}}{\partial x} \approx \frac{\mathbf{M}|_{i+1,j} - \mathbf{M}|_{i,j}}{\Delta x} = 0$$

and hence at the boundary i:

$$\mathbf{M}|_{i,j} = \mathbf{M}|_{i+1,j} \tag{20}$$

Application to other boundaries in the material involves similar implementation, and using backward differences for the opposite interfaces.

iii) Update the effective field $\mathbf{H}^n_{eff}([\mathbf{M}^n]^r)$ using the computed values of $\mathbf{M}^n$ for the next iteration. The internal, Maxwell's field is computed using:

$$\mathbf{H}^n([\mathbf{M}^n]^r) = \mathbf{B}^n/\mu_0 - [\mathbf{M}^n]^r$$

End iterations.

4) Evaluation of $\mathbf{M}^{n+1/2}$ using extrapolation: $\mathbf{M}^{n+1/2} = 2\mathbf{M}^n - \mathbf{M}^{n-1/2}$.

5) Evaluation of $\mathbf{M}^{n+1/2}$ at the locations of the $\mathbf{B}^{n+1/2}$ using two-point spatial interpolations, as described earlier, to evaluate the magnetic field from:

$$\mathbf{H}^{n+1/2} = \mathbf{B}^{n+1/2}/\mu_0 - \mathbf{M}^{n+1/2}$$

6) Finally, evaluation of the electric field $\mathbf{E}^{n+1}$ using Equation (15).

The number of iterations r in the above algorithm was controlled to satisfy the convergence criterion that $\overline{|\mathbf{M}^r|}/\overline{|\mathbf{M}^{r-1}|} - 1 \leq \zeta$ where the overbars indicate spatial averages over the magnetic material, and ζ is a small number set equal to 1×10^{-6} in this work. This convergence criterion was satisfied using 2–6 iterations, and values of ζ less than 1×10^{-6} made negligible difference to the results. This scheme was found to be stable and limited only by the Courant stability limit of the FDTD method imposed by Equation (17).

The exchange field is evaluated using the second-order accurate, central difference approximation:

$$\mathbf{H}_{ex}|_{i,j} \approx \frac{2A}{\mu_0 M_s \Delta x^2} \left\{ \begin{array}{l} \mathbf{M}|_{i+1,j} + \mathbf{M}|_{i-1,j} + \mathbf{M}|_{i,j+1} \\ + \mathbf{M}|_{i,j-1} - 4\,\mathbf{M}|_{i,j} \end{array} \right\} \tag{21}$$

The last term on the right-hand-side is due to the fact that in the two-dimensional TMz mode the magnetisation does not vary in the z-direction. Evaluation of the exchange field using Equation (21) at the magnetic material boundaries requires magnetisation values in free space on one side of the boundary which do not exist. This would yield incorrect values of the exchange field at the magnetic material boundaries. To overcome this, the value of the exchange field at the boundaries is calculated from extrapolation using the two nearest grid points inside the magnetic material. For example, the exchange field on the left-hand boundary in Fig. 2 would be evaluated using:

$$\mathbf{H}_{ex}|_{i,j} = 2\mathbf{H}_{ex}|_{i+1,j} - \mathbf{H}_{ex}|_{i+2,j}$$

In the TMz mode, the FDTD method yields two magnetic field components, while the LLG equation yields all three magnetisation vector components which are invariant in the z-direction.

4. NUMERICAL EXAMPLE: SUB-NANOSECOND MAGNETIC SWITCHING IN A THIN RECTANGULAR FERROMAGNETIC PRISM

To understand the fast switching dynamics in thin ferromagnetic films, time resolved, magneto-optical pump-probe techniques were developed [16, 17] where a fast pump laser is used to induce sub-nanosecond currents in transmission lines upon which a thin ferromagnetic film is placed. A DC field is applied parallel to the film plane to pin the slow moving domains and the pulsed fringing fields of the transmission lines perturb the in-plane magnetisation in the thin-film sample. A probe laser beam is then used to sense the magnetisation reorientation through the Kerr effect. The domain rotation dynamics are complicated not only by the magnetic properties of the sample including anisotropy and exchange, but also by the magnetodynamics due to the shape, dimensions, electrical and dielectric properties of the magnetic and other materials in the film stack. The spatial and temporal distributions of the source fields also play an important role in affecting the switching dynamics in the magnetic sample. Hence modeling and analysis of such systems would require the simultaneous solution of Maxwell's equations and the LLG equation, which is described in this section using the FDTD-LLG scheme.

The numerical example presented here follows the experimental work described in Ref. [17] where a 50 nm thick $Ni_{81}Fe_{19}$ rectangular prism sample is subjected to a non-uniform pulse field produced by two Au tracks as shown in Fig. 3. The conductive magnetic material

is separated from the Au tracks by a 10 nm thick Al_2O_3 insulating layer. The ferromagnetic sample has saturation magnetisation $M_s = 800\,\text{kA/m}$ [17], assumed uniaxial magnetocrystalline anisotropy in the x-direction with field $H_k = 875\,\text{A/m}$ [17] ($K_u = 440\,\text{J/m}^3$), exchange constant $A = 1\times10^{-11}\,\text{J/m}$, electrical conductivity $\sigma = 1\times10^7\,(\Omega\text{m})^{-1}$ and relative permittivity $\varepsilon_r = 12$ [5, 8]. The damping coefficient was set to $\alpha = 0.01$ [17]. The Au tracks have electrical conductivity $\sigma = 4\times10^7\,(\Omega\text{m})^{-1}$, relative permittivity $\varepsilon_r = 6.9$, and relative permeability of free space, $\mu_r = 1$. Typical parameters for the Al_2O_3 insulating layer are $\sigma = 1\times10^{-16}\,(\Omega\text{m})^{-1}$, $\varepsilon_r = 9.9$ and $\mu_r = 1$.

The extended length of the magnetic prism in the z-direction in Fig. 3 compared to its cross-section produces strong shape anisotropy and therefore saturates the magnetisation along the z-axis. This means that the change in magnetisation will mainly be in the x-y plane due to the pulse field. Moreover, the transmission line tracks normally extend beyond the magnetic sample. This permits the use of a two-dimensional TMz grid to model this system as the fields are invariant in the z-direction. In practice, the transmission line is dispersive causing variation in the current and hence magnetic field along the length of the tracks. This leads to variations of the magnetisation along the length of the magnetic sample. However, the effect of these variations on the magnetisation dynamics is expected to be negligible due to the strong shape anisotropy and the pinning DC field. In addition, the dynamic parameters in such experiments are normally measured over a volume of the magnetic sample which averages out the variations in the magnetisation that might occur due to the dispersive transmission lines [17].

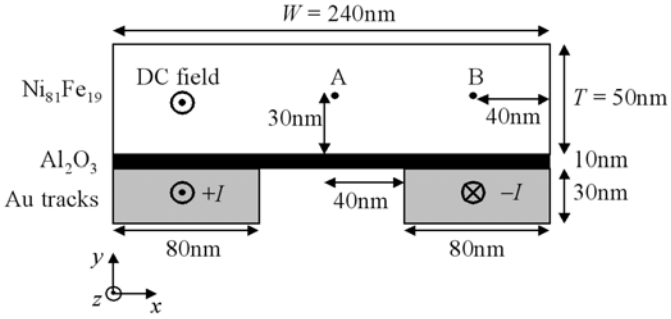

Figure 3. Geometry and dimensions of simulated thin-film Permalloy structure and transmission line. Points A and B inside the magnetic material are selected to study the vector magnetisation response to the non-uniform pulse field.

For a thin ferromagnetic film, it can be shown, following [18], that the Bloch and Neel wall widths, D, are given approximately (when $H_k \ll \mu_0 M_s$) by:

$$D = 2\pi\sqrt{\frac{A}{\mu_0 M_s^2}} \tag{22}$$

Using the $Ni_{81}Fe_{19}$ parameters gives a value $D = 22\,\text{nm}$. Hence a Yee cell with square sides of size $\Delta x = 10\,\text{nm}$ smaller than the domain wall width was chosen to discretise the simulation space. The corresponding time step that satisfies the Courant stability criterion in (17) is $\Delta t = 1.67 \times 10^{-17}\,\text{s}$. The simulation space was terminated by a 5 cell PML.

A DC field was applied in the positive z-direction of magnitude 17 kA/m (210 Oe), parallel to the direction of initial magnetisation. The initial conditions for the magnetisation were $M_x = M_y = 0$ and $M_z = M_s$. The pulse field, generated by the two transmission lines is non-uniform, and predominately vertical in the middle of the film plane (point A), and predominately in-plane directly above the centre of the conductors (point B). This particular magnetisation and field configurations enable the derivation of linearised analytical solutions to the LLG equation, which allow the validation and interpretation for the FDTD-LLG numerical results. The rate of change of the z-component of the magnetisation is also very small in this configuration and causes negligible eddy currents, which are not computed in TMz mode.

The current flowing in the transmission line can be specified as a z-directed current density in the TMz grid. However, the diverging electric fields in the FDTD grid deposit a persistent charge on the surface of the conductors even after the source is removed, thus producing non-physical fields [19]. To avoid these non-physical fields, the magnetic fields at the surfaces of the conductor (surrounding the E_z fields in the TMz grid) are instead specified. The peak field at the surfaces of the conductors was set to $h_{peak} = 499\,\text{A/m}$ (6 Oe). The corresponding current I flowing in the conductors then follows from Ampere's law $\mathbf{H} = \oint \mathbf{I} \cdot d\mathbf{L}$ and is equal to 0.1 mA.

The temporal profile of the pulse field generated by the transmission line was taken as a variant of the Gamma distribution for simplicity and since it resembles the experimental current profile in Ref. [17]. This function is shown in Fig. 4 and is given by:

$$\mathbf{h}(t) = h_{peak}\frac{t}{\tau_d}e^{(1-t/\tau_d)} \tag{23}$$

where τ_d is the decay time constant of the pulse (rise time constant

$\tau_r = 0.32\tau_d$). Evaluating the Fourier transform of (23) and solving for the frequency at which the magnitude of the spectrum reduces to 10% of its maximum value, provides an estimate of the bandwidth of this signal as $f_{10} = 3/(2\pi\tau_d)$. τ_d was chosen here to be equal to 65 ps yielding a bandwidth $f_{10} = 7$ GHz and hence propagating waves in space with minimum wavelength of around 41 mm. These waves were sampled correctly by the choice of $\Delta x = 10$ nm. The length of the simulation was chosen as 1.5 ns to allow the pulse field transients to die out as shown in Fig. 4.

4.1. Numerical Results

The FDTD-LLG algorithm was programmed in the Matlab® environment, and the field and magnetisation distributions at 400 time instances were stored over the 1.5 ns simulation length (i.e., every 3.76 ps). Fig. 5 illustrates the calculated magnetisation distribution (arrow plot) and contours of magnetic field magnitude generated by current and magnetic sources at three instances of time of the applied transient field.

As the transient field increases to its maximum value, slight deviations of the magnetisation from the saturated z-direction occur over the cross-section of the prism in the x-y plane to follow the magnetic fields from the transmission lines as shown in Fig. 5(b). The trajectory of the vector magnetisation at points A and B is shown in

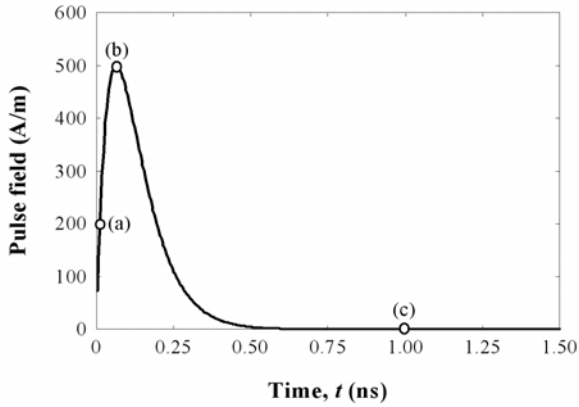

Figure 4. Gamma distribution function used to model the pulsed field from the transmission lines with decay time of 65 ps (rise time constant 21 ps). Points (a), (b) and (c) are selected time instances where the magnetisation and magnetic field distributions are plotted in Fig. 5.

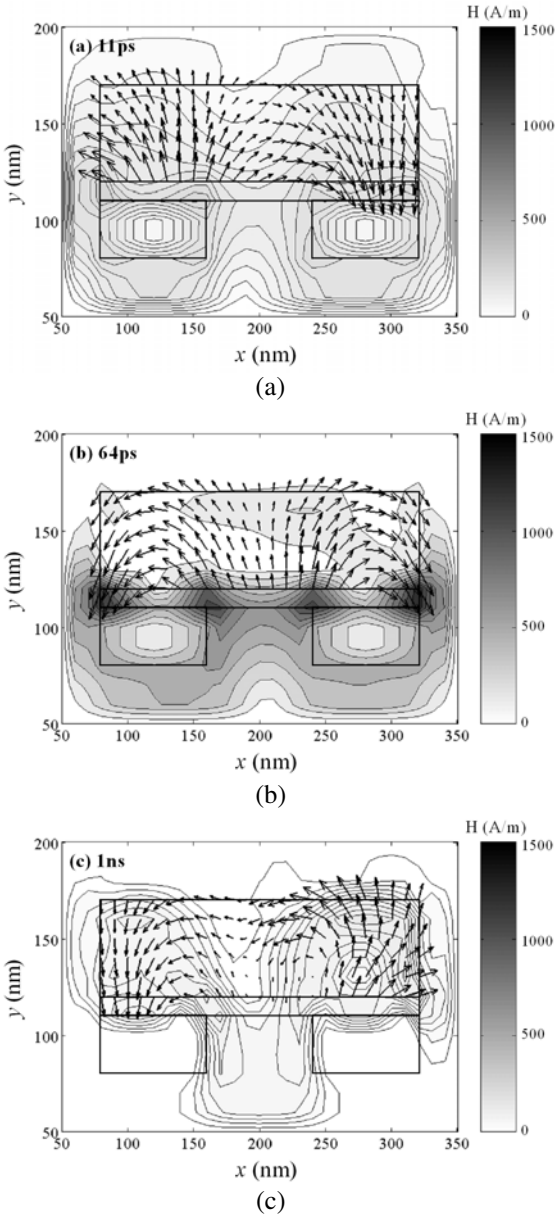

Figure 5. Magnetisation (arrow plot) and magnetic field magnitude (contour plot) distributions at three time instances: (a) 0.01 ns, (b) 0.064 ns and (c) 1 ns. Two point interpolations were carried out on the magnetic field components to evaluate them at the same location of the magnetisation. The PML region is not shown in these plots.

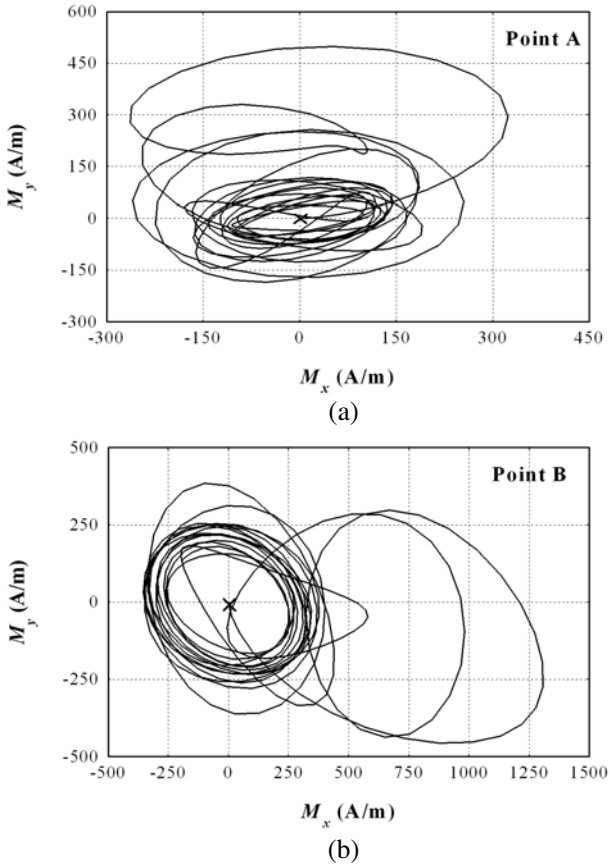

Figure 6. Trajectory of the vector magnetisation at points (a) A and (b) B, over the length of the simulation (1.5 ns). The '×' marks the initial state of the magnetisation.

Fig. 6. The strong vertical demagnetising fields force the magnetisation in the plane of the magnetic material leading to the elliptical trajectory of the magnetisation at point A as shown in Fig. 6(a). Along with the vertical demagnetising fields, point B also experiences demagnetising fields from the poles on the right-hand end of the magnetic material, leading to reduction of the ellipticity of the magnetisation trajectory with almost circular precession as indicated in Fig. 6(b).

Figure 5(c) shows evidence of non-uniform spin-waves that are clearly visible in the x-direction, as the transient fields from the transmission line diminish. The spin-resonance and spin-wave frequencies can be analysed from the Fourier transform of the temporal

change of the magnetisation and will be carried out in the next section and compared to linearised analytical solutions of the LLG equation.

4.2. Analytical Solutions to the LLG Equation

The aim of this section is to develop an approximate analytical description of the magnetisation dynamics for the system in Fig. 3. This is to confirm the validity of the numerical calculations of the combined FDTD-LLG technique, and help in their interpretation.

The strong shape anisotropy in the magnetic geometry of Fig. 3 forces the magnetisation in the z-direction and hence M_z may be written as $M_z(t) = M_s + m_z(t)$ where m_z is a small perturbation of the magnetisation in the z-direction. The small changes in the remaining magnetisation components are $M_x = m_x(t)$ and $M_y = m_y(t)$. By approximating the rectangular prism in Fig. 3 by an elliptic cylinder with cross-section defined by W and T, the demagnetising fields can be evaluated, assuming uniform magnetisation, using $\mathbf{H} = -\mathbf{NM}$, where $\mathbf{N}$ is the demagnetising factor given respectively in the x and y directions by [20]:

$$N_x = T/(W+T) \tag{24a}$$
$$N_y = W/(W+T) \tag{24b}$$

where $N_x + N_y = 1$.

The magnetic material in Fig. 3 experiences a vector pulse field $\mathbf{h}(t)$ that is approximately vertical or y-directed in the centre of the magnetic material (between the transmission lines), and approximately horizontal or x-directed in the region directly above the centre of each Au track. Each of these cases will be treated separately using uniform magnetisation in the analytical theory, to predict the dynamic behaviour of the magnetisation at points A and B.

4.2.1. y-directed Field (Point A)

Considering first the y-directed transient field between the transmission lines, the effective field components including the applied and demagnetising fields are (anisotropy field is neglected since $2K_u/\mu_0 M_s^2 \ll 1$):

$$\begin{aligned} H_x^{eff}(t) &= -N_x m_x(t) \\ H_y^{eff}(t) &= -N_y m_y(t) + h_y(t) \\ H_z^{eff}(t) &= H_z \end{aligned}$$

Substituting this effective field into the LLG equation in (7) and ignoring second and higher order perturbation terms (including

products of **m** and **h**) yields the following set of linear differential equations:

$$\frac{dm_x(t)}{dt} \approx |\gamma| \{-\alpha H_{zx} m_x(t) + M_s h_y(t) - H_{zy} m_y(t)\} \quad (25a)$$

$$\frac{dm_y(t)}{dt} \approx |\gamma| \{\alpha [M_s h_y(t) - H_{zy} m_y(t)] + H_{zx} m_x(t)\} \quad (25b)$$

$$\frac{dm_z(t)}{dt} \approx 0 \quad (25c)$$

where $H_{zx} = H_z + N_x M_s$ and $H_{zy} = H_z + N_y M_s$. When the contribution of the magnetocrystalline anisotropy is not negligible, then N_x in Equation (25) may be replaced by $N_x + 2K_u/\mu_0 M_s^2$. Taking the Laplace transform of the system of equations in (25), using the initial conditions $m_x(0) = m_y(0) = m_z(0) = 0$, yields the Laplace transforms of the magnetisation components written in transfer function notation, with $h_y(s)$ being the input field transform, as:

$$\frac{m_x(s)}{h_y(s)} = \frac{|\gamma| M_s s}{s^2 + \alpha |\gamma| (2H_z + M_s) s + \omega_0^2} \quad (26a)$$

$$\frac{m_y(s)}{h_y(s)} = \frac{|\gamma| M_s}{s + \alpha |\gamma| H_{zy}} \left\{ \alpha + \frac{|\gamma| H_{zx} s}{s^2 + \alpha |\gamma| (2H_z + M_s) s + \omega_0^2} \right\} \quad (26b)$$

where second and higher order values of α were neglected compared to unity. This transfer function form is convenient as it directly reveals information about the natural frequency of the system, its stability and state of damping, independent of the input field. The spin-resonance frequency in (26) is given by:

$$\omega_0 = |\gamma| \sqrt{H_{zx} H_{zy}} \quad (27)$$

From the Laplace transform of (25c), the solution for the perturbed z-component of the magnetisation is $m_z(t) = m_z(0) = 0$, and hence $M_z \approx M_s$. Substituting the values of M_s, H_z and N_x and N_y for the geometry in Fig. 3 yields a resonance frequency $\omega_0 = 7.16 \times 10^{10}$ rad/s or $f_0 = 11.4$ GHz.

4.2.2. x-directed Field (Point B)

When the transient field is in the plane of the material along the x-direction in the region above the tracks, the effective field components are given by (again the anisotropy field is neglected since $2K_u/\mu_0 M_s^2 \ll$

1):

$$H_x^{eff}(t) = -N_x m_x(t) + h_x(t)$$
$$H_y^{eff}(t) = -N_y m_y(t)$$
$$H_z^{eff}(t) = H_z$$

Following the same procedure in deriving Equations (25), a linearised set of ordinary, first-order coupled differential equations can be produced given by:

$$\frac{dm_x(t)}{dt} \approx |\gamma| \left\{ \alpha \left[M_s h_x(t) - H_{zx} m_x(t) \right] - H_{zy} m_y(t) \right\} \quad (28a)$$
$$\frac{dm_y(t)}{dt} \approx |\gamma| \left\{ -M_s h_x(t) + H_{zx} m_x(t) - \alpha H_{zy} m_y(t) \right\} \quad (28b)$$
$$\frac{dm_z(t)}{dt} \approx 0 \quad (28c)$$

Taking the Laplace transform of the system of equations in (28), using the initial conditions $m_x(0) = m_y(0) = m_z(0) = 0$, yields the following transfer functions:

$$\frac{m_x(s)}{h_x(s)} = \frac{|\gamma| M_s}{s + \alpha |\gamma| H_{zx}} \left\{ \alpha + \frac{|\gamma| H_{zy} s}{s^2 + \alpha |\gamma| (2H_z + M_s) s + \omega_0^2} \right\} \quad (29a)$$
$$\frac{m_y(s)}{h_x(s)} = \frac{-|\gamma| M_s s}{s^2 + \alpha |\gamma| (2H_z + M_s) s + \omega_0^2} \quad (29b)$$

The solution to (28c) is $m_z(t) = m_z(0) = 0$ and hence $M_z \approx M_s$ as expected.

The penetration of the magnetic fields produced by the transmission lines into the conductive magnetic material (and hence skin depth) is difficult to estimate due to the dynamic nature of the susceptibility and non-uniform fields. The complex dynamic susceptibility tensor $||\chi||$ may be estimated from the theory in this section by setting $s = j\omega$ in Equations (26) and (29). The equivalent dynamic susceptibility can then be found by setting $||\chi||\mathbf{h} = \eta\mathbf{h}$ and determining the eigenvalues η [21], which are simply given by $m_x(\omega)/h_x(\omega)$ and $m_y(\omega)/h_y(\omega)$ for the x-directed and y-directed fields respectively. The magnitude of this equivalent susceptibility ranges from unity at low frequencies to 200 at resonance. The skin depth, d, of the propagating magnetic fields inside the Permalloy can then be estimated from the classical skin depth equation for a highly conductive medium $d = 1/\sqrt{\pi f_{10} \mu_0 \mu_r \sigma}$ using μ_r over the range of equivalent susceptibilities and $f_{10} \sim 7\,\text{GHz}$ for the frequency of propagating fields determined by the field source. This yields skin depths in

the range 0.1–1 μm which are large compared to the thickness of the magnetic material. This means that there is negligible attenuation of the propagating magnetic fields from the transmission lines inside the Permalloy. This simplifies the process of theoretically determining the magnitude of the fields at points A and B, and enables comparison to the numerical calculations of the FDTD-LLG scheme.

The theoretical values of $m_x(t)$ and $m_y(t)$ can be determined from solving the differential equations in (25) and (28) analytically, or

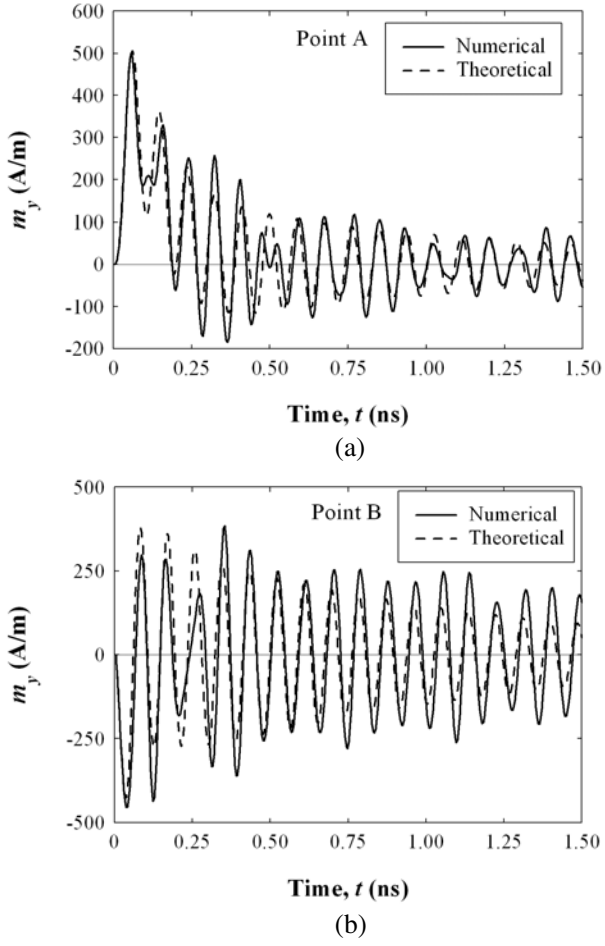

Figure 7. Numerical and theoretical temporal profiles of the y-component of magnetisation at locations (a) A and (b) B, inside the magnetic material.

from inverse Laplace transforms of the transfer functions in (26) and (29). With the large skin depth compared to the magnetic material thickness, the Biot-Savart law can be used to determine the magnitude of the fields at points A and B. Using circular conductors for simplicity, the fields outside the conductors carrying opposite current $I = 0.1\,\mathrm{mA}$ are given by [22]:

$$H_x(x', y') = \frac{-y'I}{2\pi}\left(\frac{1}{\rho_2^2} - \frac{1}{\rho_1^2}\right) \tag{30a}$$

$$H_y(x', y') = \frac{I}{2\pi}\left(\frac{x' + \rho/2}{\rho_2^2} - \frac{x' - \rho/2}{\rho_1^2}\right) \tag{30b}$$

where $\rho_1 = \sqrt{(x' - \rho/2)^2 + y'^2}$ and $\rho_2 = \sqrt{(x' + \rho/2)^2 + y'^2}$. x' and y' are the horizontal and vertical distances from the centre line between the two conductors respectively, and ρ is the horizontal separation between the centres of the two conductors. Using Equation (30b), the peak vertical transient field at point A was evaluated to be $270\,\mathrm{A/m}$, and from (30a) the peak horizontal transient field at point B was calculated to be $260\,\mathrm{A/m}$. For illustration, Fig. 7 shows only the computed time waveforms for m_y at points A and B from the FDTD-LLG scheme, and from Equations (26b) and (29b) using inverse Laplace transforms. There is good agreement between the numerical and theoretical values, thus confirming the validity of the FDTD-LLG computations and the negligible effect of skin depth. The differences in amplitude and phase between the numerical and theoretical calculations are due to the non-uniform source fields and the effects of exchange and demagnetising fields of the rectangular prism in the numerical simulations, that were either ignored or simplified in the theoretical treatment.

The uniform and non-uniform precession modes in the FDTD-LLG calculations were investigated by computing the Fast Fourier Transform (FFT) of the magnetisation waveform at point A in Fig. 7(a). The spectrum is shown in Fig. 8 and clearly reveals the spin-resonance peak at frequency 11.4 GHz, as correctly predicted by (27). The additional peaks in the spectrum of the FDTD-LLG calculations can be attributed to non-uniform spin-wave modes which are visible in Fig. 5(c). The theoretical treatment of spin-waves in ferromagnetic conductive media is complex and requires the simultaneous solution of Maxwell's equations and the LLG equation [23]. A simpler approach may be used by ignoring dissipation and damping and assuming a wave-like solution to the perturbed magnetisation in the LLG equation with no damping in the form [24]:

$$\mathbf{M} = (m_{x0}\mathbf{x} + m_{y0}\mathbf{y})e^{j(\omega t - kx)} + M_s\mathbf{z} \tag{31}$$

where only spatial variations of the magnetisation in the x-direction were considered for simplicity, with wave vector k. m_{x0} and m_{y0} are the magnitudes of the magnetisations in the x and y directions respectively. The effective field components now include exchange fields, and using (9), are given by:

$$H_x^{eff}(t) = -N_x m_x(t) + \frac{2A}{\mu_0 M_s^2}\frac{\partial^2 m_x(t)}{\partial x^2}$$
$$H_y^{eff}(t) = -N_y m_y(t) + \frac{2A}{\mu_0 M_s^2}\frac{\partial^2 m_y(t)}{\partial x^2}$$
$$H_z^{eff}(t) = H_z$$

Substituting (31) and the effective fields into the LLG equation with no damping and eliminating m_{x0} and m_{y0} yield the dispersion relation:

$$\omega = |\gamma| \sqrt{\left(H_{zx} + \frac{2A}{\mu_0 M_s}k^2\right)\left(H_{zy} + \frac{2A}{\mu_0 M_s}k^2\right)} \tag{32}$$

where $kW = p\pi$ with p being a positive integer representing the spin-wave mode, and W is the width of the magnetic material shown in Fig. 3. For the unpinned exchange boundary condition considered in this work and represented by Equation (11) (i.e., no

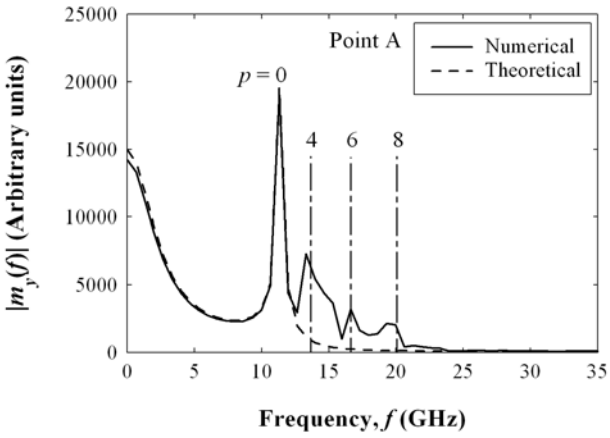

Figure 8. Numerical and theoretical spectra of magnetisation m_y computed from the Fourier transforms of the waveforms in Fig. 7(a). The spin resonance peak is shown clearly at 11.4 GHz ($p = 0$). The dash-dotted lines indicate the first few spin-wave even harmonics which occur at frequencies 13.7 GHz ($p = 4$), 16.6 GHz ($p = 6$), and 20.34 GHz ($p = 8$).

surface anisotropy), p is in general even [25]. The theoretical even harmonics, including the zeroth or spin-resonance mode, evaluated using (32) are indicated in Fig. 8 and show good correspondence with the observed peaks in the calculated spectrum from FDTD-LLG simulations. This demonstrates the ability of the FDTD-LLG scheme to model and simulate the spin-wave dynamics of complex structures with conductive and dielectric losses and different exchange boundary conditions. Analysis of allowed spin-wave modes for the rectangular prism in Fig. 3 is beyond the scope of this paper and can be found elsewhere [26, 27]. The low frequency content of the spectra of m_y in Fig. 8 is shaped by the spectrum of the transient field given by Equation (23).

5. DISCUSSION AND CONCLUSIONS

5.1. The FDTD-LLG Scheme

This paper presents an efficient approach for integrating the LLG equation into the FDTD grid whereby the vector magnetisation was located at the grid cell corners. This implementation provides simple and more accurate two-point interpolations to evaluate the magnetisation and fields at different locations within the Yee cell, and applies to two and three-dimensional grids. The complete algorithm for the solution of the non-linear system of Maxwell's and LLG equations was described making use of a stable, iterative numerical scheme for the implicit time integration of the LLG equation. A numerical example of ferromagnetic resonance in a Permalloy rectangular prism excited by a transient field from a transmission line was used to implement the FDTD-LLG scheme in TMz mode, and produced the dynamic distribution of magnetisation and magnetic fields inside and outside the material. The outcomes of the numerical simulations were in good agreement with simplified theoretical solutions of the LLG equation in uniform and non-uniform precession modes, indicating the validity of the numerical simulations.

The good agreement between the numerical simulations and theory were mainly allowed by the large skin depth of the propagating fields compared to the thickness of the magnetic material, thus permitting the use of magnetostatics to theoretically predict the magnitude of the source fields. When the frequency of the propagating fields increase and/or the thickness of the conductive magnetic material becomes comparable to the skin depth, then the use of magnetostatics to predict the magnitude of source fields, as normally carried out in pure micromagnetic studies, is no longer appropriate. In this case, the use of the FDTD method to predict the dynamic interior

fields becomes necessary, and particularly important for studying the effects of eddy currents on the switching behaviour of magnetic devices such as magnetic recording heads operating at very high frequencies. In addition to the dynamic fields from current sources, the FDTD method also naturally produces the 'self' demagnetising fields due to the magnetisation distribution inside magnetic materials, which is a computationally intensive process in pure micromagnetic calculations [28]. Moreover, fields generated by magnetic layers in the FDTD-LLG method naturally couple with other conductive and dielectric structures in the simulation space (which can have frequency-dependant constitutive parameters) to allow modelling and simulation of complete devices, with lumped circuit elements [1], which is not feasible in pure numerical micromagnetics.

One drawback of the FDTD scheme is the very small time step, and hence long simulation times, dictated by the Courant stability requirement when modeling small structures similar to those considered in this paper. The long simulations times may be reduced by using an implicit time marching scheme for the solution of Maxwell's equations that is not sensitive to the Courant limit [29]. Alternatively, and for the purpose of steady-state micromagnetic computations where the transient electromagnetic details are not important, larger time steps can be used within the iterative scheme for the integration of the LLG equation, while at the same time keeping the Courant limited time step for the solution of Maxwell's Equations [9]. This has the effect of increasing the speed of convergence of the solution to the LLG equation, and thus allowing the reduction of the simulation time.

A more logical approach to integrating the LLG equation within the FDTD framework that does not require spatial interpolations would be to employ an unstaggered, and collocated grid where all discrete vector fields and magnetisations are located at the same point in space. Direct discretisation of Maxwell's equations using central differences in an unstaggered grid yields, however, a numerically dispersive grid [30], that is not appropriate for studying dynamic wave propagation phenomena or wave interaction with magnetic material.

5.2. Unstaggered Schemes

Two non-dispersive unstaggered schemes based on Maxwell's equations (compared to schemes based on the vector potential formulation [31, 32] which are not considered here) were investigated briefly for their suitability for the FDTD-LLG scheme; the non-symmetric unstaggered (NS) scheme, and the Fourier based pseudo-spectral time-domain (PSTD) method. The NS scheme [30] uses forward and backward finite differences for the spatial derivatives of the electric and magnetic

fields in Maxwell's equations, with the nodal weights being calculated to achieve the required discretisation accuracy. The non-symmetrical nature of this discretisation scheme, however, causes inaccurate computation of the fields at interfaces between materials having relatively large differences in electrical and/or magnetic properties (for example metal/air interface). This error may be reduced by increasing the length of the stencils in the forward and backward differences or by using polynomial grading of the electrical conductivity at the interfaces, which increases the complexity of the implementation particularly for thin, multi-layer materials. In the PSTD scheme [33], spatial derivatives along each direction are approximated by discrete Fourier and inverse Fourier transforms, and hence all electric and magnetic field components are collocated in space. The difficulty with this scheme appear as unwanted oscillations (or Gibbs phenomenon) in the computed fields in the presence of electrically conducting structures or interfaces between materials with relatively large differences in electrical and/or magnetic properties. These field oscillations, even when small, alter the local fields inside the magnetic material and hence yield incorrect magnetisation distributions within magnetic structures. The Gibbs effect may be reduced through the use of non-uniform grids [34] at the expense of increased difficulty in implementation particularly for complex geometries.

This brief investigation reveals that the use of unstaggered grids would require special treatment to the spatial grids to deal with material structures having relatively sharp changes in their electric and/or magnetic properties. This would increase the complexity of the implementation particularly when modeling complex material structures with multi-layers. Thus the efficient implementation presented in this paper, while maintaining the advantages of the FDTD method, provides a simple approach for integrating the micromagnetic details of magnetic material within the FDTD formulation.

ACKNOWLEDGMENT

This work was supported in part by the Engineering and Physical Sciences Research Council under Grant GR/S46161/01.

REFERENCES

1. Taflove, A. and S. C. Hagness, *Computational Electrodynamics: The Finite-difference Time-domain Method*, 2nd edition, Arctech House, Boston, Mass., 2000.

2. Kunz, K. S. and R. J. Luebbers, *The Finite Difference Time Domain Method for Electromagnetics*, Chap. 15.3, 308–322, CRC Press, Florida, 1993.
3. Pereda, J. A., L. A. Vielva, A. Vegas, and A. Prieto, "An extended fdtd method for the treatment of partially magnetized ferrites," *IEEE Trans. Magn.*, Vol. 31, 1666–1669, 1995.
4. Pereda, J. A., L. A. Vielva, A. Vegas, and A. Prieto, "A treatment of magnetized ferrites using the FDTD method," *IEEE Microwave and Guided Wave Letters*, Vol. 3, No. 5, 136–138, 1993.
5. Pereda, J. A., L. A. Vielva, M. A. Solano, A. Vegas, and A. Prieto, "FDTD analysis of magnetized ferrites: Application to the calculation of dispersion characteristics of ferrite-loaded waveguides," *IEEE Trans. Microwave Theory and Techniques*, Vol. 43, No. 2, 350–357, 1995.
6. Zheng, G. and K. Chen, "Transient analysis of microstrip lines with ferrite substrate by extended FD-TD method," *Int. J. of Infrared and Millimeter Waves*, Vol. 13, No. 8, 1115–1125, 1992.
7. Reineix, A., T. Monediere, and F. Jecko, "Ferrite analysis using the finite-difference time-domain (FDTD) method," *Microwave and Optical Technology Letters*, Vol. 5, No. 13, 685–686, 1992.
8. Okoniewski, M. and E. Okoniewska, "FDTD analysis of magnetized ferrites: A more efficient algorithm," *IEEE Microwave and Guided Wave Letters*, Vol. 4, No. 6, 169–171, 1994.
9. Vacus, O. and N. Vukadinovic, "Dynamic susceptibility computations for thin magnetic films," *Journal of Computational and Applied Mathematics*, Vol. 176, 263–281, 2005.
10. Soohoo, R. F., *Magnetic Thin Films*, Chap. 10.2, 188, Harper and Row, New York, 1965.
11. Soohoo, R. F., *Magnetic Thin Films*, Chap. 11.1, 206, Harper and Row, New York, 1965.
12. Brown, W. F., *Micromagnetics*, Robert E. Krieger Publishing Co., New York, 1978.
13. Yee, K. S., "Numerical solution of initial boundary value problems involving maxwell's equations in isotropic media," *IEEE Transactions on Antennas and Propagations*, Vol. 14, No. 3, 302–307, 1966.
14. Berenger, J., "A perfectly matched layer for the absorption of electromagnetic waves," *Journal of Computational Physics*, Vol. 114, 185–200, 1994.
15. Slodicka, M. and I. Cimrak, "Numerical study of nonlinear ferromagnetic materials," *Applied Numerical Mathematics*, Vol. 46,

95–111, 2003.

16. Hicken, R. J. and J. Wu, "Observation of ferromagnetic resonance in the time domain," *J. Appl. Phys.*, Vol. 85, No. 8, 4580–4582, 1999.
17. Wu, J., N. D. Hughes, J. R. Moore, and R. J. Hicken, "Excitation and damping of spin excitations in ferromagnetic thin films," *Journal of Magnetism and Magnetic Materials*, Vol. 241, 96–109, 2002.
18. Soohoo, R. F., *Magnetic Thin Films*, Chap. 4.2, 40, Harper and Row, New York, 1965.
19. Wagner, C. L. and J. B. Schneider, "Divergent fields, charge, and capacitance in FDTD simulations," *IEEE Trans. Microwave Theory and Techniques*, Vol. 46, No. 12, 2131–2136, 1998.
20. Osborn, J. A., "Demagnetizing factors of the general ellipsoid," *Physical Review*, Vol. 67, No. 11–12, 351–357, 1945.
21. Soohoo, R. F., *Microwave Magnetics*, Chap. 7.1, 166, Harper & Row, New York, 1985.
22. Smythe, W. R., *Static and Dynamic Electricity*, 2nd edition, Chap. 7.09, 270, McGraw-Hill, New York, 1950.
23. Soohoo, R. F., *Magnetic Thin Films*, Chap. 11.1(a), 205, Harper and Row, New York, 1965.
24. Soohoo, R. F., *Microwave Magnetics*, Chap. 7.3, 174, Harper & Row, New York, 1985.
25. Soohoo, R. F., *Microwave Magnetics*, Chap. 7.4, 178, Harper & Row, New York, 1985.
26. Park, J. P., P. Eames, D. M. Engebretson, J. Berezovsky, and P. A. Crowell, "Spatially resolved dynamics of localized spin-wave modes in ferromagnetic wires," *Phys. Rev. Lett.*, Vol. 89, No. 27, 277201, 2002.
27. Gubbiotti, G., M. Conti, G. Carlotti, P. Candeloro, E. D. Fabrizio, K. Y. Guslienko, A. Andre, C. Bayer, and A. N. Slavin, "Magnetic field dependence of quantized and localized spin-wave modes in thin rectangular magnetic dots," *J. Phys.: Condens. Matter*, Vol. 16, 7709–7721, 2004.
28. Aharoni, A., *Introduction to the Theory of Ferromagnetism*, 2nd edition, Chap. 11, 238, Oxford Science Publications, Oxford, 2000.
29. Zheng, F., Z. Chen, and J. Zhang, "A finite-difference time-domain method without the courant stability conditions," *IEEE Microwave and Guided Wave Letters*, Vol. 9, No. 11, 441–443, 1999.
30. Liu, Y., "Fourier analysis of numerical algorithms for the maxwell

equations," *J. of Computational Physics*, Vol. 124, 396–416, 1996.

31. Kunz, K. S. and R. J. Luebbers, *The Finite Difference Time Domain Method for Electromagnetics*, Chap. 19.3, 360, CRC Press, 1993.
32. De, Flavis, F., M. G. Noro, R. E. Diaz, G. Franceschetti, and N. G. Alexopoulos, "A time-domain vector potential formulation for the solution of electromagnetic problems," *IEEE Microwave and Guided Wave Letters*, Vol. 8, No. 9, 310–312, 1998.
33. Liu, Q. H., "The PSTD algorithm: A time-domain method requiring only two cells per wavelength," *Microwave and Optical Technology Letters*, Vol. 15, No. 3, 158–165, 1997.
34. Leung, W. and Y. Chen, "Transformed-space nonuniform pseudospectral time-domain algorithm," *Microwave and Optical Technology Letters*, Vol. 28, No. 6, 391–396, 2001.